JGR Atmospheres

Key Points:
- Anvil clouds are driven toward a favored structure at which they undergo strong radiative heating and have a positive radiative effect
- Clouds prone to radiative destabilization have higher concentrations of ice crystals
- The properties of aged cirrus may depend on the time of day at which they were detrained

Tropical Anvil Clouds: Radiative Driving Toward a Preferred State

Adam B. Sokol[1] [ID] and Dennis L. Hartmann[1] [ID]

[1] Department of Atmospheric Sciences, University of Washington, Seattle, WA, USA

Abstract The evolution of anvil clouds detrained from deep convective systems has important implications for the tropical energy balance and is thought to be shaped by radiative heating. We use combined radar-lidar observations and a radiative transfer model to investigate the influence of radiative heating on anvil cloud altitude, thickness, and microphysical structure. We find that high clouds with an optical depth between 1 and 2 are prevalent in tropical convective regions and can persist far from any convective source. These clouds are generally located at higher altitudes than optically thicker clouds, experience strong radiative heating, and contain high concentrations of ice crystals indicative of turbulence. These findings support the hypothesis that anvil clouds are driven toward and maintained at a preferred optical thickness that corresponds to a positive cloud radiative effect. Comparison of daytime and nighttime observations suggests that anvil thinning proceeds more rapidly at night, when net radiative cooling promotes the sinking of cloud top. It is hypothesized that the properties of aged anvil clouds and their susceptibility to radiative destabilization are shaped by the time of day at which the cloud was detrained. These results underscore the importance of small-scale processes in determining the radiative effect of tropical convection.

Plain Language Summary Clouds play an important role in Earth's energy balance, especially in the tropics. Thick clouds cool the climate by reflecting sunlight, while thinner clouds located high in the atmosphere warm the climate due to their strong greenhouse effect. Tropical thunderstorms generate expansive cloud systems ("anvil" clouds) that initially exert a cooling effect but evolve over time to produce a warming effect. Their net impact on the climate system depends on how much time they spend in their cooling and warming stages. In this study, we use satellite measurements and a radiation model to examine how anvil clouds evolve. We find that anvil clouds with a climate-warming effect are pervasive in the tropics and can be found far from any thunderstorm that would have produced them, suggesting that they are maintained in their warming stage for long periods of time. We observe some unique characteristics of these clouds that provide clues about the processes that maintain them. Our findings provide real-world support for previous hypotheses that, until now, relied on computer simulations. They also highlight the importance of small-scale processes in shaping the large-scale tropical energy balance and underscore the need to consider these processes in projections of future climate change.

1. Introduction

Convective clouds play an important role in the energy budget of the tropical atmosphere. Mesoscale convective systems (MCSs) consisting of deep, rainy convective cores and detrained anvil clouds reflect incoming shortwave (SW) radiation and trap outgoing longwave (LW) radiation emitted by Earth's surface and lower atmosphere. These SW and LW effects are individually strong but nearly cancel each other out on climatological scales. As a result, the net cloud radiative effect (NCRE) in tropical convective regions is near zero (Harrison et al., 1990; Hartmann et al., 2001; Ramanathan et al., 1989). Despite longstanding knowledge of this cancelation, questions remain about its very nature and susceptibility to change. There are compelling reasons to deepen our understanding of convection's radiative balance: Changes to the balance would themselves constitute an important climate feedback (Hartmann, 2016) and could alter patterns in sea surface temperature (Wall et al., 2019), convective aggregation (Bretherton et al., 2005; Wing & Emanuel, 2014), and atmospheric circulation and precipitation (e.g., Randall et al., 1989; Voigt & Shaw, 2015).

The radiative neutrality of tropical convection owes itself to the widespread presence of moderately thick anvil clouds. These clouds exhibit a weakly positive NCRE but are long lasting and horizontally expansive,
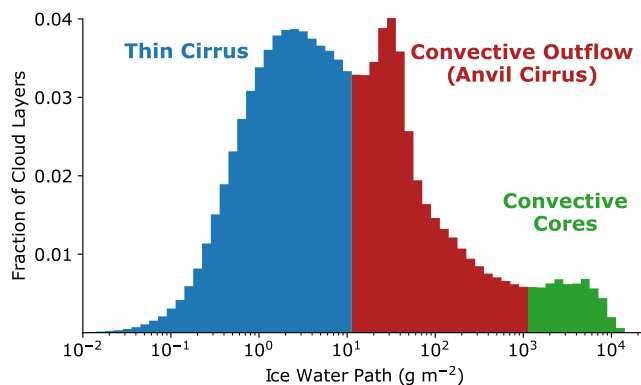
Figure 1. Histogram of the ice water path (IWP) of individual cloud layers with tops above 10 km in the tropical western Pacific (12°S to 12°N, 150–180°E). Three cloud types are identified for heuristic purposes using the histogram's two relative minima as boundaries. Layer IWP is calculated using the cloud retrievals described in section 2.1.1 prior correcting for the diurnal cycle of lidar sensitivity (see section 2.1.2). Bin widths are 0.1 in log space.

allowing them to balance the strongly negative NCRE exhibited by deep convective cores and optically thick anvil clouds over a smaller area (Hartmann & Berry, 2017). The pervasiveness of moderately thick anvils is evident in the observed distribution of ice water path (IWP) of high cloud layers over the western Pacific warm pool (Figure 1). The distribution suggests three cloud layer categories: deep convective cores, convective outflow (anvil cirrus), and the thin cirrus that are characteristic of the tropical upper troposphere. The monotonic increase in frequency as IWP decreases from 10^3 to ∼30 g m^{-2} represents the flattening and horizontal spreading of anvil clouds after they are detrained (Lilly, 1988). If this thinning and spreading were to continue indefinitely, one would expect to observe a continued increase in frequency as IWP declines from 30 g m^{-2} to the limit of cloud detection. Rather, the distribution peaks at ∼30 g m^{-2} before falling and rising again to the thin cirrus mode at ∼2 g m^{-2}. This existence of a peak at 30 g m^{-2} suggests that anvil clouds are preferentially maintained at that point. Similar bimodality has previously been observed in the Southeast Asian monsoon region (Berry & Mace, 2014), but its causes remain largely unexplored. To understand how the anvil cloud distribution may change in the future, it is necessary to understand the processes that govern the evolution of convective outflow.

Radiative heating has long been recognized as an important driver of anvil cloud dynamics (Ackerman et al., 1988; Lilly, 1988). Optically thick anvil clouds undergo strong LW heating near cloud base and cooling at cloud top, which leads to destabilization and in-cloud convective mixing (Dobbie & Jonas, 2001; Schmidt & Garrett, 2013). Solar heating of cloud top during the day works against this destabilization but is generally weaker in magnitude than LW heating (Ackerman et al., 1988). Optically thin cirrus are heated throughout by both LW and SW; this generates buoyancy and drives a mesoscale circulation that lofts the cloud with respect to its clear-sky surroundings and promotes lateral spreading (Dinh et al., 2010; Durran et al., 2009). The importance of radiatively driven motions in the anvil cloud life cycle is supported by cloud-resolving model simulations showing that anvil lifetimes are substantially prolonged by radiative heating (Dobbie & Jonas, 2001; Gasparini et al., 2019; Hartmann et al., 2018). However, the relative importance of in-cloud convection and mesoscale lofting remains unclear.

Recent work has helped to better understand the connections between radiative heating, anvil cloud evolution, and the climatological NCRE of tropical convection. Hartmann and Berry (2017) hypothesized that radiative heating plays a critical role in driving the convective cloud population toward one that results in the observed near-neutral NCRE. Their hypothesis, which we refer to as the selective cloud maintenance hypothesis, posits that the LW heating dipole in optically thick anvil clouds acts to thin them until the vertical gradient in cloud radiative heating is strong enough to incite in-cloud convection, which maintains the cloud at an optical thickness corresponding to a positive NCRE. This maintenance of positive-NCRE anvils balances the negative NCRE exhibited during the earlier stages of the MCS life cycle. The selective cloud maintenance hypothesis was further explored by Hartmann et al. (2018), who found that radiatively driven turbulence maintains moderately thick anvil clouds by vertically recycling water vapor. In-cloud updrafts promote ice growth by vapor deposition, drive new ice crystal nucleation, and counteract sedimentation. The water vapor supply is then replenished by the sublimation of ice crystals in descending air parcels. The strength of this "microphysical cycling" mechanism is sensitive to changes in the model microphysical scheme, and the importance of fresh ice crystal nucleation is particularly unclear. Other simulations have found nucleation to play a lesser role in cloud maintenance (Gasparini et al., 2019), and aircraft measurements of anvil clouds in the eastern Pacific found only a couple of cases in which ice crystal concentrations were reflective of nucleation events (Jensen et al., 2009).

The selective cloud maintenance hypothesis and microphysical cycling mechanism have yet to be validated by observations. Previous observational studies have used geostationary satellite measurements to track the radiative evolution of individual MCSs (Wall et al., 2018) and spaceborne radar retrievals to examine anvil vertical structure (Yuan et al., 2011). In both of these studies, instrumental limitations prevented the detection of certain cloud properties that are important to the evaluation of anvil cloud maintenance mechanisms.

In situ observations (e.g., Heymsfield et al., 2002; Jensen et al., 2009) have provided important insights into anvil cloud vertical structure but are limited in amount and scope.

The objective of this study is to characterize the microphysical and macrophysical evolution of tropical anvil clouds using the observational tools necessary to capture their entire life cycle. In doing so, we evaluate the selective cloud maintenance hypothesis, the relative importance SW and LW radiative heating, and the plausibility of microphysical cycling. In section 2, we describe the satellite data and methodologies that are used to identify anvil clouds and deep convective cores, calculate radiative heating rates, and examine anvil cloud evolution. Results are presented in section 3 and discussed in section 4. We summarize our findings and discuss their implications in section 5.

2. Data and Methodology

In this section, we describe the data and methodologies used to identify anvil clouds and deep convective cores. We then discuss how composites of thinning anvils are constructed and used to calculate radiative heating rates.

We use observations from several instruments aboard satellites belonging to the A-train constellation (Stephens et al., 2002), which follows a Sun-synchronous orbit that crosses the equator at approximately 01:30 and 13:30 local time (which we also refer to as night and day, respectively). This allows for the comparison of daytime and nighttime cloud populations but precludes the study of how individual anvil clouds evolve over time. Geostationary satellite measurements have been used in the past to examine the MCS life cycle (Wall et al., 2018), but these passive sensors fail to capture optically thin anvil clouds and cannot provide information about vertical structure, both of which are necessary to evaluate anvil maintenance processes. A-train observations are obtained for the full 2009 calendar year apart from two periods for which data are unavailable (16 February to 12 March and 8 to 31 December).

We consider two tropical maritime regions extending from 12°S to 12°N: the Indian Ocean (IO; 55–95°E) and the West Pacific (WP; 150–180°E). These two regions both have a small climatological NCRE despite frequent deep convection (Harrison et al., 1990; Ramanathan et al., 1989), and MCSs in both regions tend to be aggregated into large complexes consisting of several convective cores with connected anvil cloud decks (Yuan & Houze, 2010). This stands in contrast to the nearby Maritime Continent region, in which MCSs are frequent and extensive but tend to be separated from one another. In order to restrict our analysis to maritime convection, we exclude observations from the southern tip of the Indian subcontinent that falls within the bounding box of the IO region.

2.1. Anvil Clouds

2.1.1. Satellite Retrievals

A-train hosts the Cloud-Aerosol Lidar and Infrared Pathfinder Satellite Observations (CALIOP) instrument aboard the CALIPSO satellite and the Cloud Profiling Radar (CPR) aboard the CloudSat satellite. Berry and Mace (2014) demonstrated that both instruments are needed to detect the full spectrum of radiatively active cirrus in tropical convective regions. The sensitivity of CALIOP to small ice crystals allows it to detect thin cirrus clouds and the tenuous tops of thicker cloud layers. However, because the lidar signal becomes fully attenuated at an optical depth of 4–5, it is unable to capture the full extent of optically thick clouds (Winker et al., 2010). Those clouds are better captured by the CloudSat radar's longer wavelength, which is sensitive to large ice crystals but does not detect the smaller ones seen by CALIOP. The coincident radar and lidar observations offered by the A-train constellation can thus be synergistically used to detect cloudy volumes with a wide range of optical properties.

We obtain combined CloudSat-CALIPSO observations from two DARDAR (raDAR-liDAR) data products. As described in Delanoë and Hogan (2008), the DARDAR algorithm combines CALIOP and CPR measurements using a variational scheme that estimates ice cloud properties for cloudy volumes detected by both instruments and for those detected by only one instrument. When both instrument are available, two independent pieces of information are known about the cloud particle size distribution, which allows the retrieval to rely less on empirical, a priori estimates than it does for regions detected by only one instrument. The DARDAR grid has a vertical resolution of 60-m and ~1.1-km horizontal spacing between profiles. More than 4.2 million profiles are used in this study (57% from the IO region and 43% from the WP), which are about evenly split between day and night.
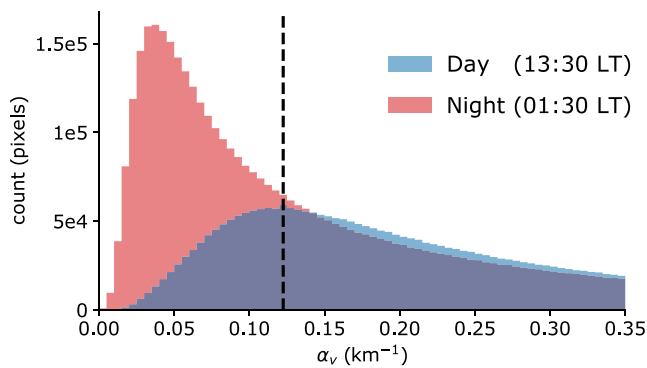
Figure 2. Histograms of visible extinction coefficient (α_v) for DARDAR-CLOUD lidar-only pixels during the (blue) 13:30 LT and (red) 01:30 LT equatorial crossings. The dashed line shows the threshold used to correct for the diurnal variation in lidar sensitivity. The histograms use data from the WP and IO study regions for the full month of May 2009.

Cloud layer information and ice microphysical properties are obtained from DARDAR-CLOUD v2.1.1 (Delanoë & Hogan, 2010). DARDAR-CLOUD uses a vertical separation threshold of 480 m to distinguish cloud layers and provides profiles of retrieved visible extinction coefficient (α_v), ice water content (IWC), and effective radius (r_e). We further calculate the visible optical depth (τ) and IWP of each cloud layer by vertically integrating α_v and IWC, respectively. DARDAR-CLOUD has been extensively used and evaluated against in situ observations and other combined retrieval products (e.g., Deng et al., 2013; Delanoë et al., 2013; Stein et al., 2011). Nevertheless, the errors associated with the retrieval algorithm are substantial, especially in regions detected by only one instrument, and several shortcomings in the DARDAR-CLOUD version used here have been identified. The most relevant shortcoming to this study is the apparent overestimation of α_v and IWC in regions seen by the lidar alone (Deng et al., 2013), which implies that the cloud layer τ and IWP calculated in the present study may be biased high in some cases. For a more detailed discussion of the errors associated with DARDAR-CLOUD and the improvements made to reduce them, we direct the reader to Delanoë and Hogan (2010) and Cazenave et al. (2019).

In addition to the DARDAR-CLOUD retrievals, we obtain estimates of ice crystal number concentration from DARDAR-Nice v1.0 (Sourdeval et al., 2018). We use the DARDAR-Nice retrieval of the concentration of ice crystals with a maximum diameter greater than 5 μm (N_i). The N_i estimation methodology assumes a monomodal particle size distribution, which may introduce bias at temperatures above −50°C, since bimodal distributions become increasingly likely at warmer temperatures. We do not expect this to jeopardize the results of this study, which focuses primarily on N_i measurements at colder temperatures. Sourdeval et al. (2018) and Krämer et al. (2020) compared DARDAR-Nice to aircraft observations and found generally good agreement, but both noted that DARDAR-Nice overestimates N_i by a factor less than 2 for temperatures colder than −60°C. While this may affect the quantitative accuracy of the anvil N_i reported here, it does not impact our qualitative conclusions.

2.1.2. Correcting for the Diurnal Cycle of Lidar Sensitivity

Because we seek to compare daytime (13:30 LT) and nighttime (01:30 LT) observations of anvil clouds, differences in instrument sensitivity during day and night must be taken into account. The CALIOP minimum detectable backscatter is highest during the day due to background solar noise (McGill et al., 2007), which prevents the detection of tenuous cloud features that would otherwise be detected at night. This difference can be seen in Figure 2, which shows daytime and nighttime histograms of DARDAR-CLOUD α_v for pixels seen by the lidar only. The diurnal cycle of lidar sensitivity is apparent at low values of α_v, which are detected frequently at 01:30 but rarely at 13:30. The histograms show much better agreement for values of α_v exceeding the daytime modal value, which suggests a reduced impact of solar noise. Low-α_v pixels are often found at cloud edge, which complicates the comparison of 01:30 and 13:30 cloud geometries. To account for this, we remove all cloudy, lidar-only pixels from the DARDAR retrievals for which α_v is less than 0.12 km^{-1} and treat them as if they are clear sky. The threshold corresponds to the daytime modal value and is indicated by the dashed black line in Figure 2. The correction removes 21.5% of daytime lidar-only pixels and 49.0% of nighttime lidar-only pixels, which has important implications for the detection of properties such as cloud-top height (CTH) and geometric thickness. On average, cloud layer top height is reduced by 126 and 333 m during day and night, respectively. Despite this, the impact of the correction on cloud layer τ is negligible, since the affected pixels contribute relatively little to the layer-integrated α_v. The implications of the correction on cloud fraction statistics are discussed in section 3.1.

2.1.3. Anvil Identification

For the purposes of this paper, we use the term "anvil cloud" to refer to high ice cloud layers that are likely produced by deep convection. After low-α_v pixels have been removed to correct for the diurnal bias in lidar sensitivity, we identify the uppermost four cloud layers in each profile using the DARDAR cloud layer index. A layer is classified as an anvil cloud if it meets the following three criteria:

1. The layer CTH exceeds 10 km. This excludes midlevel convection from our analysis and corresponds to the minimum CTH used by Berry and Mace (2014) in their definition of cirrus layers.
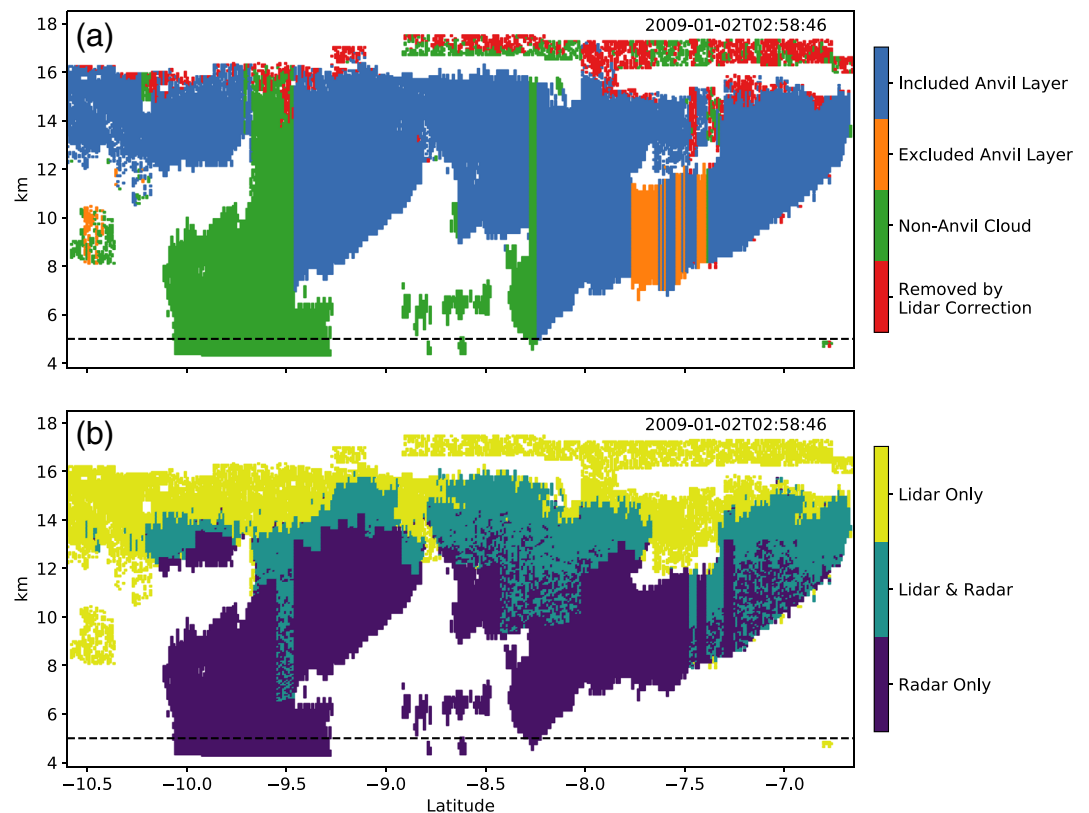
Figure 3. Example DARDAR-CLOUD scene from the West Pacific region. (a) Results of our anvil identification algorithm showing (blue) anvil cloud layers included in our analysis, (orange) anvil layers excluded from analysis because they are not the uppermost anvil layer in the column, (green) nonanvil layers, and (red) cloudy pixels that did not meet the minimum extinction threshold required by the lidar sensitivity correction. (b) Availability of lidar and radar measurements. The dashed black line at the 5-km level indicates the minimum cloud base height permitted for anvil layers.

2. The layer cloud base height (CBH) exceeds 5 km, which corresponds to the average freezing level in the study regions as calculated from reanalysis temperature included in DARDAR-CLOUD (originally from the European Centre for Medium-Range Weather Forecasts). This criterion is intended to exclude deep convective cores, which have bases near the surface.

3. The layer IWP exceeds $10\,\mathrm{g\,m^{-2}}$. This threshold corresponds to the relative minimum between the two cirrus modes of the layer IWP distribution (Figure 1), and we therefore expect that it carries physical meaning. Of course, it is possible that some thin anvil layers are wrongly excluded by this criterion and that some thick cirrus that are not of convective origin are wrongly included, but we expect these cases to be small in number compared to our sample size.

Anvil layers found beneath nonanvil cirrus layers are included in our analysis but those found beneath other anvils are not, so that no more than one anvil layer from each vertical profile is included in our analysis.

The results of the anvil identification methodology for a typical scene are shown in Figure 3a. This example demonstrates the ability of the three criteria to distinguish cirrus layers connected to deep convection from thin cirrus of unknown origin, such as the uppermost cloud layer present in the right-hand half of the scene. Limitations of our methodology are also apparent. As an example, consider the lowermost cloud layer near 7.5° S, which is classified as an anvil cloud in some profiles but not in others. When the vertical separation between this layer and the overlying one is less than 480 m, a single anvil layer is identified that extends from ~7 to ~15 km. When the separation exceeds 480 m, two distinct layers are identified, and the lower one is excluded from analysis. Because our methodology considers each profile individually, it cannot account for nuances such as these that are apparent when the profile is viewed within its larger context. We have inspected more cloud scenes and found that scenarios such as the one discussed here are rare, and we do not expect this limitation to have significant impacts on our results.

Figure 3b shows which portions of the cloud scene are detected by the CALIPSO lidar and CloudSat radar and makes clear that both instruments are needed to accurately determine CTH and geometric thickness. Some thin anvil layers (such as those on the left-hand edge of the scene) would go entirely undetected if only radar observations were used. Of all anvil layers identified in this study, 72.1% are detected by both instruments (though not necessarily at the same altitude), 27.6% are detected by only the lidar, and 0.3% are detected by only the radar. This supports the conclusion of Berry and Mace (2014) that both instruments are needed to capture the full spectrum of radiatively active ice clouds. It is also evident in Figure 3b that the stretches of cloud seen by both the radar and the lidar are quite limited; this has important implications for retrieval uncertainty, for which we direct the reader to the aforementioned references.

2.2. Convective Cores

We use observations of 11-μm brightness temperature (TB_{11}) to identify deep convective cores and find the spreading distance (d_{core}) of each anvil observations from the nearest core. Because the cloud-free atmosphere is nearly transparent to infrared radiation in the 11-μm band, TB_{11} measured from space is sensitive to the presence of deep convective clouds with cold tops. Observations are provided by the Moderate Resolution Imaging Spectroradiometer (MODIS) Level 2 Cloud Product (Platnick et al., 2017). MODIS is a scanning radiometer aboard the Aqua satellite that provides plan view TB_{11} observations (channel 31) coincident with CloudSat and CALIPSO measurements. Each MODIS data granule has a swath width of 2,330 km and includes 5 min of observations, corresponding to an along-track length of about ~2,000 km. TB_{11} measurements are provided at 5 × 5-km resolution.

Different methods of convective core identification using infrared brightness temperatures have been demonstrated and discussed in the literature (e.g., Gettelman et al., 2002; Setvák et al., 2006; Young et al., 2012). Here, we use a simple TB_{11} threshold of 210 K. Any contiguous cluster of two or more MODIS pixels with TB_{11} below 210 K is considered a convective core (pixels sharing a corner are contiguous). We calculate d_{core} as the distance between each DARDAR anvil observation and the nearest core found in the colocated MODIS swath, even if the core lies outside of the study region boundaries, which is the case for ~10% of anvil observations within the study region. Values of d_{core} are invalid if they exceed the distance between the DARDAR profile and the nearest edge of the MODIS swath. Since anvils may persist far from their convective source in both space and time, we do not consider whether an anvil observation and its nearest core belong to the same contiguous cloudy region. The TB_{11} at the location of the DARDAR profile is also found using nearest-neighbor interpolation.

This method of convective core identification is susceptible to two types of errors. First, as demonstrated in Young et al. (2012), optically thick anvil clouds can be mistakenly classified as convective core when a 210-K TB_{11} threshold is used. This type of error would increase the apparent size of a core by mistakenly including some of the surrounding anvil, which would result in artificially low d_{core} values for the anvil observations associated with that core. Second, our method could fail to detect deep convective towers that do not have sufficiently cold TB_{11} signatures but nevertheless produce anvil cloud. This type of error would result in inflated d_{core} values for anvils associated with warmer cores. We inspected the d_{core} values assigned to anvil layers thicker than the 95th percentile of geometric thickness (7.74 km), which are likely to be freshly detrained and close to their convective source. Approximately one fourth of these anvil profiles are found to have d_{core} exceeding 100 km. This suggests that a nonnegligible amount of convective cores may go undetected by a 210-K threshold, which is consistent with previous findings (Young et al., 2012).

While this convective core identification methodology is relatively crude, it is sufficient for our purposes. In this study, we use d_{core} mainly to show that anvil clouds can routinely be found far away from a convective source. Errors in d_{core} values on the order of tens of kilometers are inconsequential for these purposes, since MCSs can extend horizontally for hundreds of kilometers. Detailed analyses of MCS structure require a more precise method of core identification such as those used by Yuan and Houze (2010) and Igel et al. (2014).

2.3. Anvil Cloud Composites and Radiative Heating

The cloud observations from A-train satellites are instantaneous snapshots, which precludes us from examining how anvil clouds evolve over time. Instead, we composite the anvil cloud profiles using τ as the basis, since it is tightly linked to cloud radiative heating and the hypotheses we seek to evaluate. To generate composites of thinning anvils, each observation is first assigned to one of four groups based on region (WP or IO)

and time of day (01:30 or 13:30). The anvil profiles within each group are binned by $\log_{10} \tau$ using a bin width of 0.1, and statistics are obtained for each bin.

Anvil τ generally decreases with time after detrainment due to horizontal spreading, precipitation, and ice crystal sedimentation. However, because the initial τ of freshly detrained anvils likely varies from storm to storm, it is possible that a particular anvil was detrained more recently than an optically thicker one detected at the same moment in time. Furthermore, the typical lifetime of convectively generated cirrus can regularly exceed the 12 hr between the two daily A-train overpasses (Luo & Rossow, 2004; Mace et al., 2006). It is then likely that many of the aged, optically thin cirrus detected at 13:30 were detrained during the preceding night, and vice versa. For these reasons, it should be remembered that the composites presented here simply reflect the anvil population at the time of the two A-train overpasses and are not necessarily representative of how individual cloud systems evolve over time.

To calculate realistic cloud radiative heating rates, we must first construct profiles of IWC and r_e that are representative of the anvil clouds in each τ bin and retain their vertical structure. Because the anvil ice particle size distribution varies vertically in a characteristic way (Heymsfield et al., 2002; Yuan et al., 2011), we cannot simply average together the microphysics profiles from cloud layers at different altitudes and temperatures, since this would smear out much of the vertical structure. Instead, we generate IWC and r_e profiles using the following procedure. Within each τ bin, we select anvil profiles that have CTH within 500 m of the τ-bin median, calculate the median CBH of that subset, and keep only those profiles with CBH within 500 m of that. We then find the median IWC and r_e of the remaining profiles at each vertical level and interpolate onto the 500-m vertical grid used in the radiative heating model. The resulting profiles have retained the altitude, geometric thickness, and microphysical structure characteristic of observed anvil clouds with similar τ.

The IWC and r_e profiles for each τ bin are fed into the single-column rapid radiative transfer model for general circulation modeling (RRTMG Iacono et al., 2000; Mlawer et al., 1997). We use a surface temperature of 28°C and albedo of 0.08, 400 ppm CO_2, and average temperature, water vapor, and ozone profiles for the study region as calculated from 1989–2007 ERA-Interim reanalysis. For the 13:30 anvil profiles, we use insolation corresponding to 13:30 LT on the equinox (1,261 W m^{-2}). Ice cloud treatment follows Fu (1996) and Fu et al. (1998). Recent work has shown that cirrus cloud radiative forcing can be underestimated by radiative transfer algorithms that do not account for ice crystal surface complexity (Järvinen et al., 2018). Cirrus optical properties are also sensitive to assumptions about ice crystal habit (Wendisch et al., 2007). Detailed treatment of these issues is important for modeling the role of cirrus in global climate but is beyond the scope of this study.

Radiative heating model output is used to calculate the net heating rate, Q_R, which is equal to the sum of the SW and LW heating rates for the 13:30 observations and simply equal to the LW heating rate for the 01:30 observations. From this, we calculate the mass-averaged net heating rate for the cloud layer, $\bar{Q}_R$, which can help understand the potential for mesoscale anvil lofting. We also calculate the mass-averaged, in-cloud lapse rate tendency (LRT) due to radiative heating:

$$\left.\frac{\partial \Gamma}{\partial t}\right|_{rad} = -\frac{1}{P_B - P_T} \int_{P_T}^{P_B} \frac{\partial Q_R}{\partial z} dP, \tag{1}$$

where Γ is the lapse rate and P_B and P_T are the pressures at cloud base and top, respectively. The LRT is a measure of the destabilization produced by a vertically varying Q_R. If there is stronger heating at cloud base than at cloud top ($\partial Q_R/\partial z < 0$), the vertical column is destabilized and the LRT is positive. On the contrary, if heating is stronger at cloud top ($\partial Q_R/\partial z > 0$), the column is stabilized, and the LRT is negative.

2.4. Statistical Analysis

The procedure described up to this point generates four composites (one for each unique combination of study region and time of day) and a single profile of ice microphysics and radiative heating for each τ bin within the composites. While these profiles are realistic, they cannot capture the diversity of structures found among the ~1.35 million anvil profiles used in this study, and they do not provide a basis for statistical evaluation. To bolster the statistical robustness of our results, we randomly split each of the four groups of anvil profiles into 100 subsamples and repeat the compositing procedure and radiative heating calculations for each. The subsample sizes are equal within each of the four groups of observations but vary between

Table 1
Anvil Cloud Identification Results

	All	Day[a]	Night[b]	West Pacific	Indian Ocean
Number of profiles	4,239,774	2,119,485	2,120,641	1,808,562	2,431,212
Total cloud fraction	63.1%	63.4%	62.8%	71.4%	56.9%
Anvil cloud fraction	32.1%	33.0%	31.2%	35.0%	29.9%
Fraction of anvil cloud profiles with					
Single anvil layer (no overlying cirrus)	84.7%	80.7%	88.8%	81.8%	87.2%
Multiple anvil layers (no overlying cirrus)	3.2%	4.0%	2.3%	3.5%	2.9%
Single anvil layer with overlying cirrus	11.7%	14.7%	8.5%	14.0%	9.6%
Multiple anvil layers with overlying cirrus	0.2%	0.3%	0.1%	0.3%	0.1%
Median properties of overlying nonanvil cirrus					
Cloud-top height (km)	15.8	15.8	15.8	16.0	15.5
Thickness (km)	0.60	0.66	0.54	0.60	0.60
Optical thickness	0.12	0.12	0.11	0.11	0.12

Note. All values are calculated from DARDAR-CLOUD after the removal of low-extinction pixels as described in section 2.1.2.
[a]Data from the 13:30 LT A-train equatorial overpass. [b]Data from the 01:30 LT overpass.

the groups from 3,105 for the WP at 01:30 to 3,763 for the IO at 13:30. This resampling provides us with 100 independent microphysical and radiative heating profiles for each unique combination of τ, study region, and time of day. Composites shown in section 3 reflect the average of the 100-subsample composites within each group. The subsample composites are also used to test for significant differences in cloud properties between the 01:30 and 13:30 observations using the nonparameteric Mann-Whitney-Wilcoxon test with a two-tailed significance level of $\alpha = 0.01$. While the subsampling and large initial sample size used in this study provide a high level of statistical confidence, it is important to remember that our results remain susceptible to any biases in the DARDAR retrievals.

3. Results

We begin by discussing the results of our anvil cloud identification scheme in section 3.1. We then examine the distribution of anvil τ (section 3.2) and its evolution with spreading distance (section 3.3). In sections 3.4–3.6, we discuss anvil macrophysical structure, radiative heating, and microphysical structure, respectively.

3.1. Anvil Cloud Detection

The results of our anvil cloud identification process are provided by region and time of day in Table 1. Altogether, anvil cloud layers are identified in 32.1% of retrieval profiles. This is higher than that reported by Yuan and Houze (2010), who used a TB_{11} threshold of 260 K to identify high cloud complexes (which include anvils). We find that 56.0% of the anvil profiles identified here have interpolated MODIS TB_{11} greater than 260 K, which can explain the difference between results. This shows that many anvil clouds are sufficiently transparent to LW radiation to avoid detection by TB_{11} thresholds and has important implications for observational studies of convective cloud populations.

Anvils account for about one half of all cloud layers with tops above 10 km and bases above 5 km, which is consistent with previous findings that approximately half of the cirrus clouds in tropical convective regions are associated with deep convection (Luo & Rossow, 2004; Mace et al., 2006; Massie et al., 2002). We note, however, that the statistics in Table 1 were computed after the lidar bias correction described in section 2.1.2 was applied. Without the bias correction, the overall anvil cloud fraction would be only 0.8% higher, but the total cloud fraction would be 8.4% higher. This results in a slightly lower ratio of anvil cirrus to total cirrus but is still in line with previous findings. The difference indicates that the bias correction completely erases a substantial amount of thin, nonanvil cirrus and may not be suitable for studies of thin cirrus climatology.

Table 1 also provides information about the vertical columns in which anvil cloud layers were detected. The majority of anvil-containing profiles (84.7%) contain a single anvil layer that is the uppermost cloud
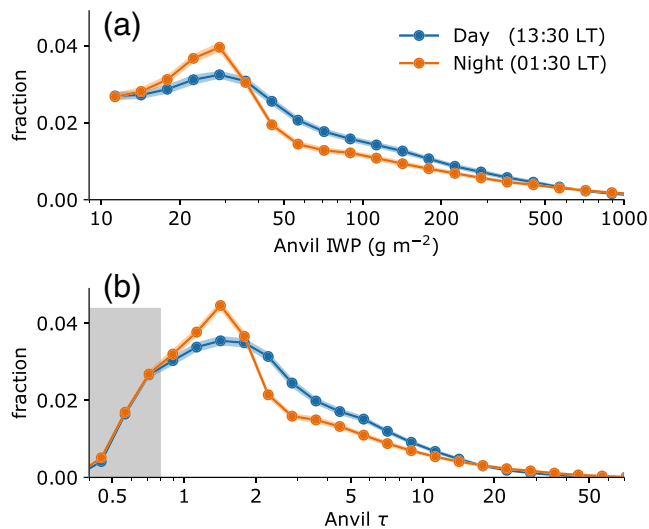
Figure 4. Anvil cloud fraction as a function of anvil (a) IWP and (b) τ at 13:30 (blue) and 01:30 (orange). Colored shading indicates the standard deviation of histograms generated by randomly splitting the data into 100 subsamples of equal size. In (b), the gray shading indicates the τ interval where the anvil fraction is artificially low due to the use of an IWP threshold of $10\,g\,m^{-2}$ during anvil identification. Measurements are combined from the WP and IO regions. IWP and τ bin widths are 0.1 in log space.

layer in the profile. The remainder contained multiple cloud layers meeting the anvil requirements (3.4%), a nonanvil layer located above the anvil (11.9%), or both (0.2%). The presence of thin cirrus clouds above thicker anvil cirrus has been previously observed and discussed (e.g., McFarquhar et al., 1999; Winker & Trepte, 1998). We find overlying cirrus to be more common during the day (15.0% of anvil-containing profiles) than at night (8.6%) and more common in the WP (14.3%) than in the IO (9.7%). Overlying cirrus are optically and geometrically thin and have a median CTH of 16.0 and 15.5 km in the WP and IO, respectively. We note that these statistics only pertain to overlying cirrus containing at least one pixel with α_v exceeding the threshold used for the lidar diurnal bias correction. The frequency of overlying cirrus reported here should therefore be interpreted as a lower bound, and the geometric and optical properties do not reflect the thinnest cirrus.

3.2. Anvil Optical Thickness

Figure 4 shows the distributions of anvil τ and IWP observed at 13:30 and 01:30. They are normalized by dividing the number of observations in each bin by the total number of retrieval profiles at 13:30 or 01:30 so that they essentially represent anvil cloud fraction as a function of IWP and τ. The colored shading indicates the standard deviation of the 100 independent subsample histograms. The subsamples show very good agreement, indicating that the distribution shape is statistically robust. There are no major differences between the WP and IO distributions (not shown).

During both times of day, the IWP distribution peaks at $\sim 28\,g\,m^{-2}$, which matches the convective outflow peak in Figure 1 and approximately corresponds to the IWP at which high ice cloud layers exert their maximum NCRE (Berry & Mace, 2014; Hartmann & Berry, 2017). As expected, the distributions of anvil τ closely resemble those of IWP and have peaks at ~ 1.4. The frequency of anvils with $\tau < 0.8$ (gray shading in Figure 4b) is artificially reduced due to our requirement that anvil clouds have an IWP greater than $10\,g\,m^{-2}$. The peak at 1.4, however, is not an artifact of our anvil identification methodology (see Text S1 and Figures S1–S3 in the supporting information). We note that while 0.3% of anvil profiles have τ exceeding 40, the figures in this paper only show results for $\tau < 40$ so that details are visible.

The anvil IWP and τ distributions show important diurnal differences. First, the 01:30 distribution contains fewer optically thick clouds with IWP between 40 and $600\,g\,m^{-2}$ ($2 \lesssim \tau \lesssim 20$) than the 13:30 distribution. Assuming that anvil IWP and τ decrease over time, this suggests that the anvil population at 01:30 is, on the whole, more aged than that at 13:30. This is consistent with the timing of the A-train equatorial crossings in relation to the diurnal cycle of deep convective activity over oceans, which has a maximum between 05:00 and 07:00 LT and a minimum in the evening hours (Nesbitt & Zipser, 2003). The 13:30 A-train overpass takes place about 7 hr after the peak in convective activity and would therefore encounter a "fresher" anvil cloud population that the 01:30 overpass, which occurs 19 hr after the peak. Second, anvils with an IWP between 20 and $35\,g\,m^{-2}$ ($1 \lesssim \tau \lesssim 2$) are more common at 01:30, but those with an even lower IWP ($10–20\,g\,m^{-2}$) are found at a similar frequency at both times of day. As a result, the distribution peak is more pronounced at 01:30 than at 13:30. This suggests that anvil clouds progress toward an optical depth of 1–2 over time but do not continue to thin as rapidly after that. We hereinafter refer to anvil clouds with τ between 1 and 2 as "modal anvils."

3.3. Anvil Spreading Distance

The distribution of anvil d_{core} across both study regions and times of day is shown in Figure 5a. The large number of anvil profiles in the lowest d_{core} bin reflects the misclassification of optically thick anvils with TB_{11} below 210 K as convective cores. Other than this, frequency initially increases with d_{core}, which is to be expected from the vertical thinning and horizontal spreading of anvil clouds as they drift radially outward from the core into a stably stratified environment (Lilly, 1988). There is a peak between 30 and 60 km, but the location of the peak is sensitive to the TB_{11} threshold used for core identification. Frequency decays
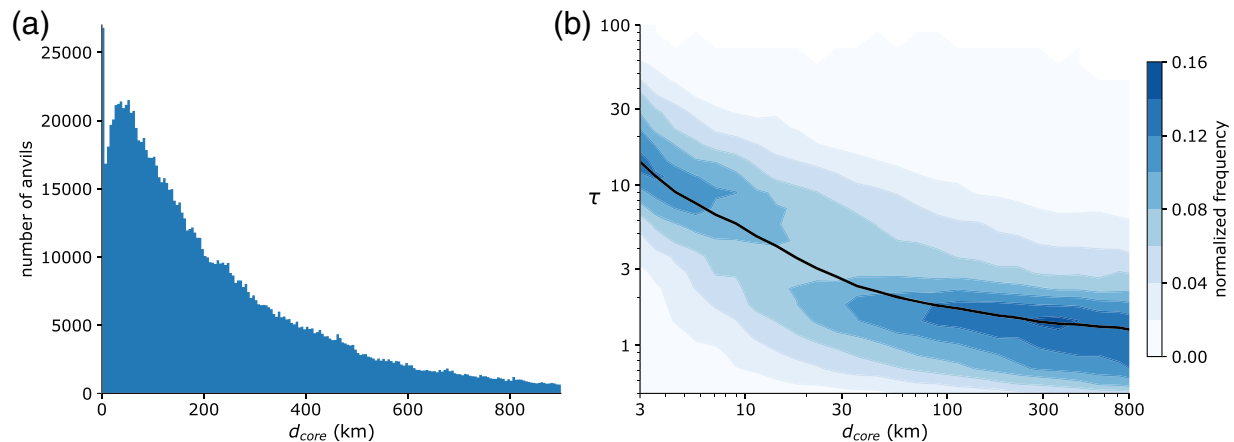
Figure 5. (a) Histogram of anvil cloud spreading distance, d_{core}, using a bin width of 5 km. (b) Joint histogram of anvil d_{core} and τ, with frequency normalized by column so that the values in each d_{core} bin add up to one. The black line indicates the median τ for each d_{core} bin. Bin widths are 0.1 in log space for both τ and d_{core}. Note that both axes use a linear scale in (a) but a logarithmic scale in (b).

exponentially beyond the peak, and approximately one third of anvil profiles are located further than 250 km from the nearest core.

The evolution of anvil τ with spreading distance can be seen in Figure 5b, which shows a joint histogram of τ and d_{core} normalized so that the sum of frequencies in each d_{core} bin is equal to 1. The black line indicates the median τ of the clouds in each d_{core} bin. Freshly detrained anvils have a median τ between 10 and 20 and are optically thicker at 01:30 than at 13:30 (Figure S4). Median τ exhibits power law decay within 40 km of the convective core, as evidenced by the linearity of the black line in Figure 5a, which has logarithmic axes. This initial optical thinning coincides with the horizontal spreading indicated by Figure 5a and proceeds more rapidly at night (Figure S4). In addition to dynamic spreading, precipitation may hasten optical thinning over this interval. Between 50 and ~300 km, median τ follows a slower power law decay regime. Modal anvils increasingly dominate the population over this interval and continue to do so at further distances.

So far, we have shown that there is a prevalence of anvil clouds with τ between 1 and 2 at both 13:30 and 01:30 and that these modal anvils are uniquely capable or persisting several hundred kilometers away from the nearest convective core. Together, these two findings support the hypothesis that anvils are driven toward and maintained at an optical thickness corresponding to a positive NCRE. They do not, however, provide insight into the mechanisms responsible for cloud maintenance. To examine those, we turn to the composites of anvil cloud macrophysical, radiative, and microphysical properties.

3.4. Macrophysical Structure

Changes in CTH and geometric thickness (calculated here as CTH-CBH) can provide further insight into the processes responsible for anvil cloud evolution and maintenance. The evolution of these properties with respect to τ is shown in Figure 6. The contour plots show the fraction of profiles in each τ bin that contain anvil cloud at a given height and thus reflect the typical height and thickness of anvils at different stages of optical thinning. Black lines indicate median CTH and CBH. Median geometric thickness is shown below the corresponding cloud fraction composites (shading shows one standard deviation). The diurnal difference in geometric thickness is statistically significant ($\alpha = 0.01$) everywhere except for $\tau \approx 6$ and $\tau \gtrsim 30$ in the IO. Anvil cloud evolution and its diurnal differences are more pronounced in the WP than in the IO but are qualitatively similar in both regions; for the sake of simplicity, any numeric values referenced in our discussion are for the WP.

We begin with freshly detrained anvils. The optically thickest anvils are detrained with similar CTH during day and night. Geometric thickness is typically between 6 and 9 km and is slightly greater at 13:30 due to the lower CBH found then. At night, cloud top sinks nearly 1 km and cloud base rises as τ decreases from 40 to 10. This results in rapid geometric thinning and is consistent with the flattening of convective outflow by positive buoyancy at cloud base and negative buoyancy at cloud top (Lilly, 1988). During the day, the postdetrainment drop in CTH is small compared to that at night, but the rise in CBH is similar. Geometric
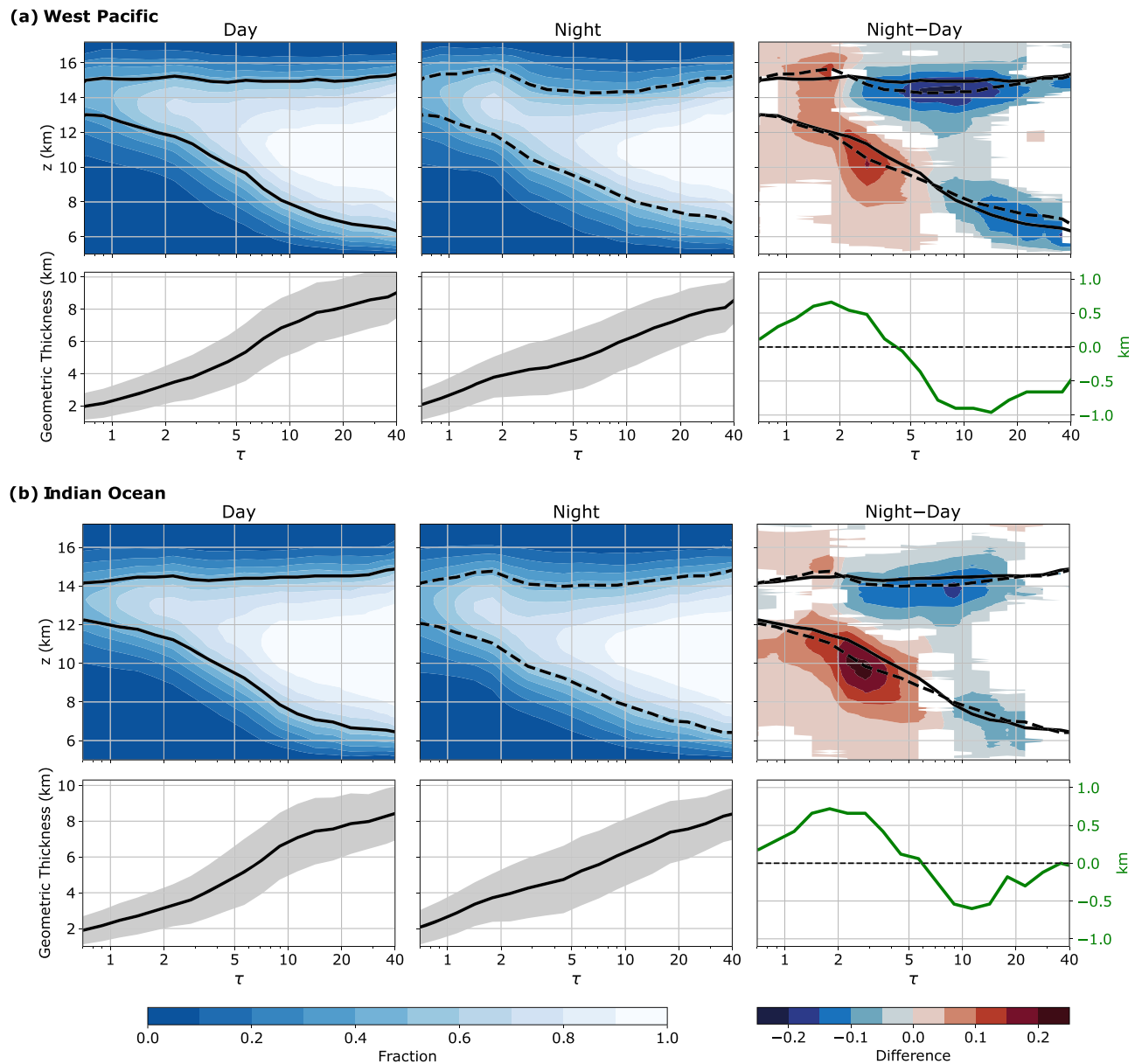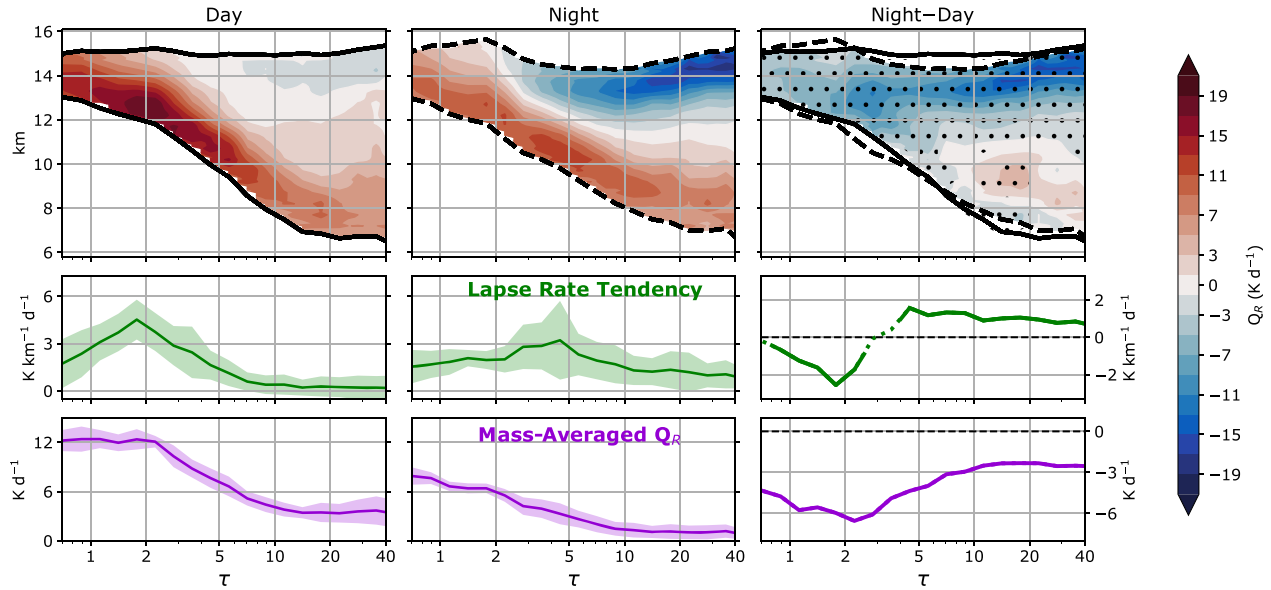
Figure 6. Anvil cloud geometry as a function of τ in the (a) West Pacific and (b) Indian Ocean regions, shown for (left) day, (middle) night, and (right) night minus day. For each region and time of day, the top plot shows the fraction of anvil cloud profiles in each τ bin that contain cloud at a given height. Black lines (solid for day and dashed for night) show median CTH and CBH. The bottom plots show median geometric thickness, with shading indicating one standard deviation. The green lines shows the difference in median geometric thickness between night and day and are plotted with a different vertical axis.

thinning is slower as a result, and daytime anvils are nearly 1 km thicker than nighttime anvils by $\tau \approx 10$. As τ decreases from 10 to 4, CTH is relatively constant at both times of day and is ~600 m lower at 01:30 than at 13:30. Geometric thinning over this interval is thus caused by the continued rise of cloud base, which is greater during the day than at night. By $\tau \approx 4$, thickness is again similar at both times of day, and nighttime anvils remain at a slightly lower altitude.

Several interesting macrophysical shifts occur as τ approaches the modal range of 1–2. At night, median CTH in the WP rises by 1.2 km as τ decreases from 4 to 1.8, where it reaches its peak value (15.7 km). This rise in CTH is nearly as large as the rise in CBH over the same interval, which results in very little geometric thinning. During the day, the rise in median CTH is more modest (~300 m to a peak value of 15.2 km at $\tau \approx 2.2$), and there is more geometric thinning. As a result, modal anvils observed during the day are ~600 m
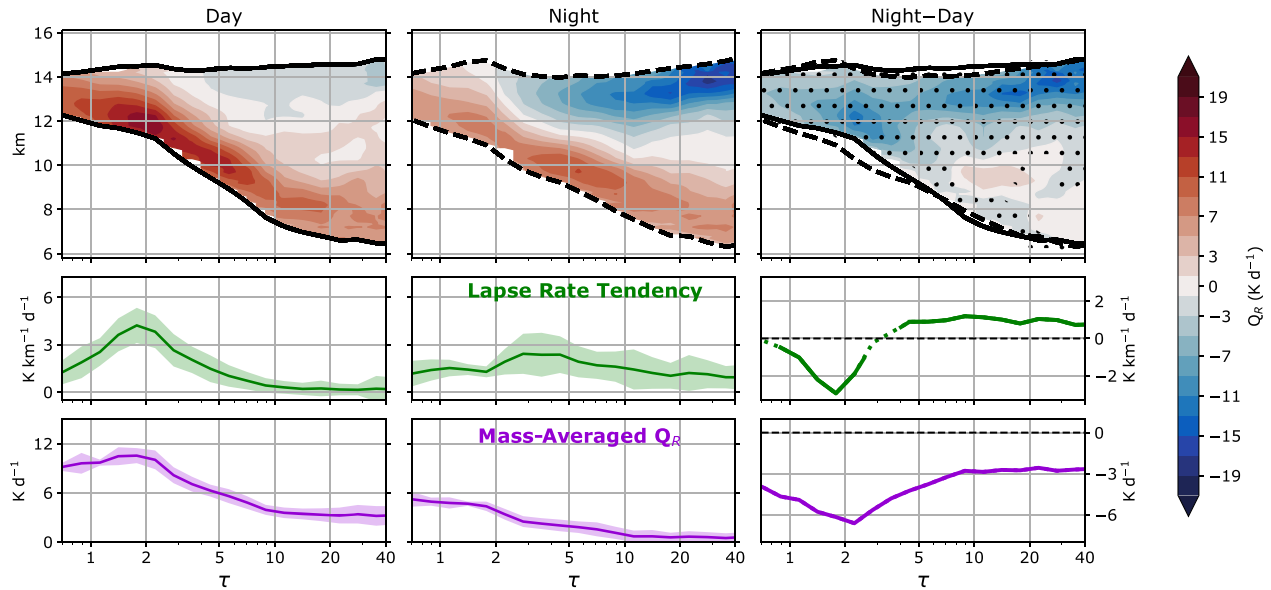
Figure 7. Net radiative heating rates for the (a) West Pacific and (b) Indian Ocean regions for (left) day, (middle) night, and (right) night minus day. For each region and time of day, the top plot shows the mean net heating rate of the 100-subsample composites. Stippling indicates a statistically significant diurnal difference ($\alpha = 0.01$), and black lines (solid for day and dashed for night) show median CTH and CBH. The middle and bottom rows show the 100-subsample mean lapse rate tendency (LRT) and mass-averaged layer heating ($\bar{Q}_R$), respectively. Shading indicates the standard deviation of the subsample composites. The lines showing night-day LRT are solid where the difference is statistically significant and dotted otherwise. The night-day $\bar{Q}_R$ is statistically significant at all τ.

thinner and have a median CTH that is ∼500 m lower than their counterparts observed at night There is also less variability in their geometric thickness: The interquartile range is 1,380 m at 13:30 compared to 1,620 m at 01:30.

It is clear from Figure 6 that the macrophysical evolution of anvil clouds differs substantially between night and day despite similar initial conditions. At night, anvil tops sink after detrainment, but modal anvils are found at high altitudes. Daytime CTH is much more constant but nevertheless reaches its maximum as τ approaches the modal range. In the next section, we examine these diurnal differences in the context of radiative heating.

3.5. Radiative Heating

Net radiative heating rates (Q_R) are shown in Figure 7 and are provided as the mean of the 100-subsample composites for each region and time of day. The spread in Q_R among the subsample composites (Figure S5) is greatest at large τ near cloud base and top, where the magnitude of Q_R is generally largest and a difference in CTH or CBH of one vertical level can have a large impact on Q_R at a fixed height. The diurnal difference in Q_R, shown in the third column of Figure 7, is statistically significant throughout most of the composite. This is to be expected from the addition of SW heating during the day, but we note that the diurnal difference in LW heating rates (not shown) is also statistically significant throughout much of the composite. Figure 7 also shows the 100-subsample mean LRT and $\bar{Q}_R$, with shading indicating the 100-subsample standard deviation. The subsamples show good agreement with respect to $\bar{Q}_R$ despite the substantial spread in Q_R at any fixed point in the composite. There is also good agreement for LRT, which shows the largest spread at night for thick clouds undergoing strong cooling at cloud top and heating at cloud base.

Upon detrainment, optically thick anvils undergo strong LW cooling at cloud top of up to 20 K day^{-1}, which contributes to the negative buoyancy at the top of the outflow plume. During the day, SW heating cancels out much of this cooling, resulting in a small Q_R. This 15-K diurnal difference in cloud-top Q_R helps explain why CTH decreases after detrainment at 01:30 but is maintained aloft at 13:30 and suggests that radiative heating plays an important role in the early stages of the anvil life cycle. During both times of day, cloud base experiences strong LW heating. While this may contribute to cloud base lofting, prior work has shown that the total diabatic heating near the base of freshly detrained anvils is likely dominated by evaporative cooling (Gasparini et al., 2019).

As τ decreases from 10 to 4 and CBH continues to rise, the temperature difference between cloud base and the surface increases. This strengthens LW heating at cloud base and drives a gradual rise in $\bar{Q}_R$ during both times of day. At night, the warming region near cloud base and the cooling region near cloud top are brought closer together as the cloud thins, which generates stronger heating gradients and causes LRT to increase. The strongest destabilization (highest LRT) occurs at $\tau \approx 4$, when cloud base heating reaches its maximum value and there is still substantial cooling near cloud top. During the day, net heating at cloud top remains small as τ decreases from 10 to 4, but $\bar{Q}_R$ and LRT continue to increase gradually. At $\tau \approx 4$, the contributions of SW and LW heating to total $\bar{Q}_R$ are approximately equal, and $\bar{Q}_R$ is nearly twice as strong as it is at night.

The heating characteristics of modal anvils are notable for several reasons. As τ drops to 2, LW cooling at cloud top ceases, at which point the anvils are heated in their entirety. As a result, modal anvils undergo stronger mass-averaged heating than their optically thicker precursors, which is demonstrated by a substantial increase in $\bar{Q}_R$. This coincides with the large increase in nighttime CTH. Furthermore, modal anvils show large, statistically significant diurnal differences in both $\bar{Q}_R$ and LRT. We examine each in turn.

The mass-averaged heating of modal anvils is nearly twice as high during the day than at night. There are two reasons for this difference. First and most importantly is SW heating, which accounts for about one third of total $\bar{Q}_R$ during the day and ~75% of the diurnal difference. The second reason, which accounts for the remaining 25%, is the diurnal difference in modal anvil geometry. Because modal anvils at 13:30 are geometrically thinner than those at 01:30 but have equal τ, they must have a higher in-cloud α_v on average. The higher α_v results in greater LW flux convergence near cloud base and thus stronger radiative heating there. In fact, the heating at modal anvil base at 13:30 is the strongest heating found anywhere. Because of this geometric effect, mass-averaged LW heating is greater during the day than at night (8.2 vs. 6.2 K day^{-1} at $\tau = 1.8$).

Modal anvils also undergo stronger radiative destabilization during the day. This is unexpected, since SW heating is generally strongest near cloud top and therefore acts to decrease LRT and stabilize the cloud. Again, cloud geometry is responsible for the diurnal difference. Destabilization is driven by LW heating, which is highest near cloud base and decreases with height. The geometric effect described in the previous paragraph produces especially strong vertical gradients in LW heating during the day, which acts to increase LRT. The LW LRT exceeds 4 K km^{-1} day^{-1}, which greatly outweighs the stabilization provided by SW heating (-0.4 K km^{-1} day^{-1}). Because of the geometric effect, LRT at $\tau = 1.8$ is twice as high during the day than at night, and the daytime peak LRT exceeds the nighttime peak at $\tau \approx 4$ by more than 40%.

In this section, we have shown that radiative heating hastens initial anvil thinning at night but hinders it during the day. As anvils evolve, they are increasingly heated and destabilized by LW radiation. Modal anvils
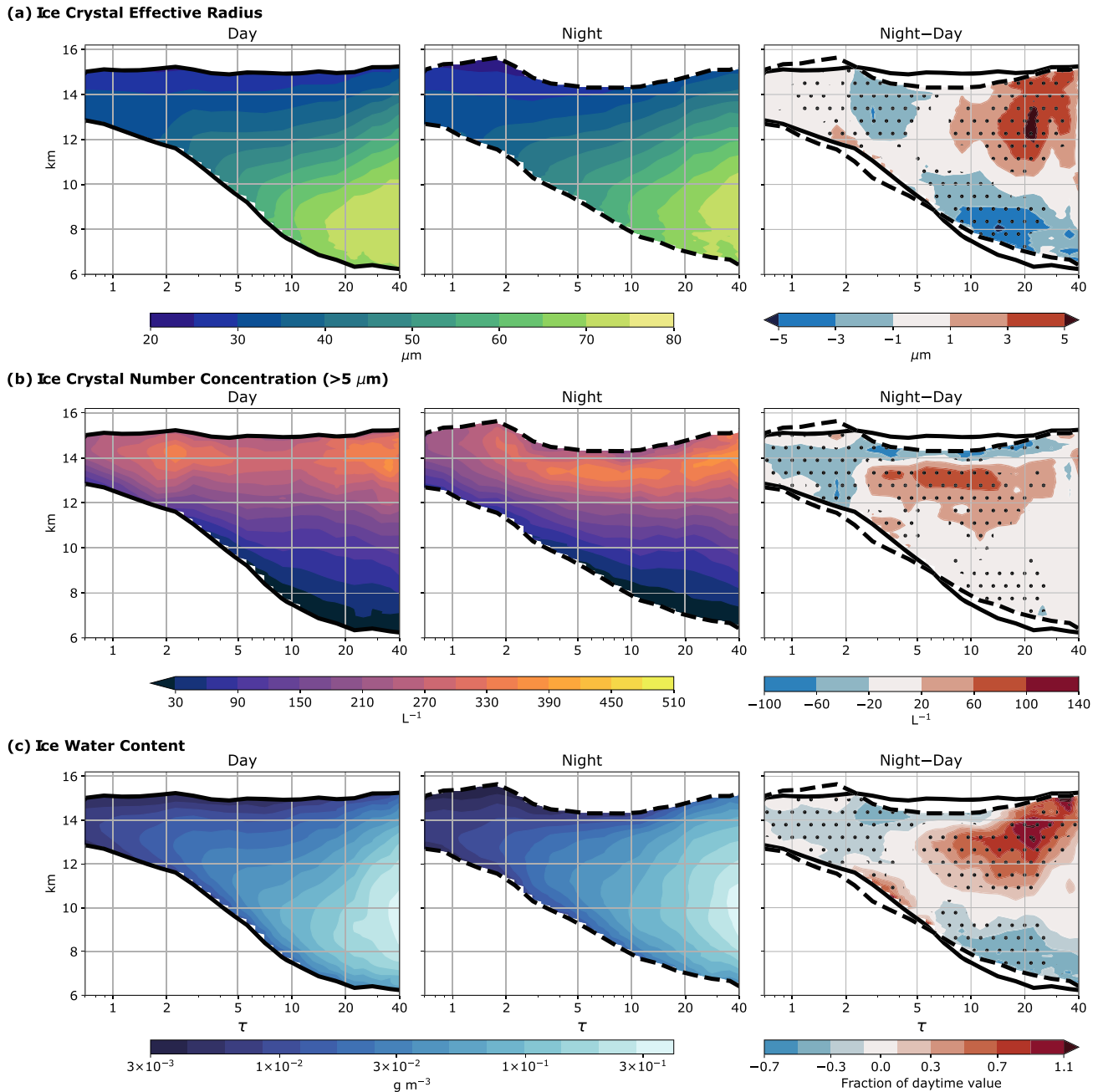
Figure 8. Composites of (a) effective radius, (b) number concentration of ice crystals with a maximum diameter exceeding 5 μm, and (c) ice water content for anvil clouds in the West Pacific for (left) day, (middle) night, and (right) night minus day. Values are the means of the 100-subsample composites. Stippling indicates a statistically significant difference between day and night. Black lines (solid for day and dashed for night) indicate median CTH and CBH. In (c), the color shading for the day and night composites uses a logarithmic scale, and the night-day difference is expressed as a fraction of the daytime value.

are too tenuous to undergo LW cooling at cloud top but still undergo substantial heating; as a result, their Q_R is higher than that of their optically thick precursors. During the day, the thinner geometry of modal anvils makes them more susceptible to LW heating and destabilization. Evidence of destabilization may also be apparent in anvil microphysical structure, which is discussed in the next section.

3.6. Microphysical Structure

The evolution of anvil microphysical structure can provide further insight into anvil maintenance mechanisms. Figures 8 and 9 show 100-subsample mean composites of r_e, N_i, and IWC. The 100 subsamples show good agreement when it comes to the median r_e, N_i, and IWC at any particular point in the composite,
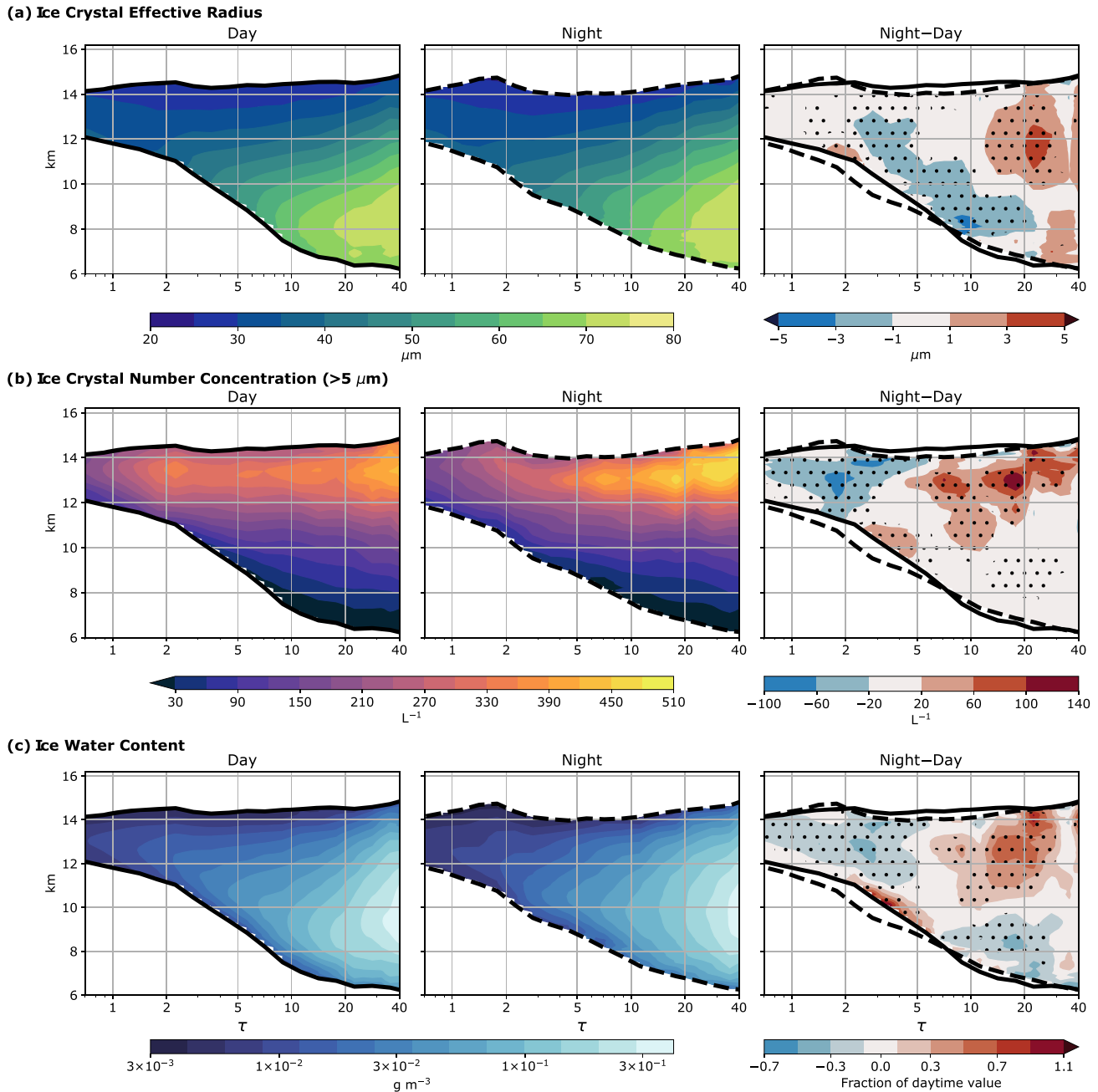
Figure 9. As in Figure 8 but for the Indian Ocean region.

but we note that there is substantial variability among the individual anvil profiles within each subsample (Figures S6 and S7). Nevertheless, the anvil cloud vertical structure found here is consistent with in situ aircraft measurements (Heymsfield et al., 2002; Jensen et al., 2009; Lawson et al., 2010; McFarquhar & Heymsfield, 1996) and satellite observations (Yuan et al., 2011). Median r_e generally decreases with altitude, as expected from gravitational size sorting and the temperature dependence of ice diffusional growth. N_i, which is dominated by smaller ice crystals, generally increases with height until its maximum ~1 km below cloud top. Despite high N_i near cloud top, maximum IWC is typically found 1–2 km above cloud base and decreases with altitude above that point, suggesting that total IWC is dominated by large ice crystals. The layer of low IWC at cloud base, sometimes accompanied by smaller r_e, likely reflects a subsaturated layer

where sublimation occurs. The vertical structure of α_v (not shown) is very similar to that of IWC; this is consistent with the finding that the radiative properties of anvil clouds are shaped primarily by large ice crystals (Jensen et al., 2009; Lawson et al., 2010).

There is large diurnal variability in the vertical structure of fresh, optically thick anvils with τ exceeding 10. They are more "top-heavy" at 01:30, in that r_e, IWC, and N_i are larger in the upper half of the cloud and smaller in the bottom half than they are at 13:30. These differences are statistically significant in many areas. Since top-heaviness would be expected to generally decrease with time as large ice crystals settle, it could be the case that optically thick anvils observed at 01:30 were detrained more recently than those observed at 13:30. It could also be the case that deep convection is more intense at night and carries large ice crystals to higher altitudes. We cannot distinguish these effects here but believe that the diurnal variability in the vertical structure of freshly detrained anvils is worthy of further study.

As τ decreases from 40 to 10, the IWC and r_e at a fixed altitude decrease substantially. In Figures 8 and 9, this appears as positively sloped contours in the upper portions of the cloud at large τ. Cloud-top N_i also decreases, although the decrease is not monotonic in every composite. This factor-of-4 decrease in τ is accompanied by a relatively small decrease in geometric thickness, suggesting that optical thinning at the initial stages of the anvil life cycle is driven primarily by microphysical changes rather than geometric changes. This could reflect anvil precipitation and is consistent with previous findings that large ice crystals are removed relatively rapidly after detrainment (Garrett et al., 2005; Jensen et al., 2018). On the whole, these changes act to reduce the initial diurnal difference in microphysical structure, though the 01:30 anvils remain more top-heavy in some respects at $\tau = 10$.

As τ falls below 10, the relative importance of geometric and microphysical thinning shifts. At this point, geometric thickness begins to decrease rapidly with decreasing τ, and the r_e and IWC contours in the upper portion of the anvil flatten out. This transition is most apparent in the 13:30 composite for the WP and is indicative of a microphysical equilibrium in which r_e and IWC remain relatively constant at a fixed altitude level. A similar equilibrium was noted by Gallagher et al. (2012) during aircraft sampling of convective outflow and was attributed to a balance between the growth of ice crystals by aggregation and their removal by sedimentation.

The evolution of cloud-top N_i as τ decreases from 10 to 2 is of particular interest. After its initial postdetrainment decrease, N_i reaches a relative minimum at some τ between 3 and 7, depending on the region and time of day. As τ reaches the modal range, there is a resurgence in N_i that is present in all of the composites but is much more pronounced during the day, when it peaks at $\tau \approx 2.2$. This coincides with the large daytime increase in radiative LRT and $\bar{Q}_R$ and the ~300-m increase in daytime median CTH. At night, when there is no notable increase in LRT at the modal τ but rather a large rise in CTH, the N_i resurgence is much less pronounced, constituting only a minor disruption to the general decrease in cloud-top N_i that accompanies optical thinning. The daytime resurgence in N_i is not sensitive to the compositing methodology described in section 2.3, in which each composite reflects the median microphysical quantities of anvil cloud profiles falling within a τ-specific CTH and CBH range. If we instead compare all 13:30 anvil profiles with CTH within a fixed range, enhanced N_i is consistently found in those with τ between ~1.5 and ~3. This ensures that the N_i signal at $\tau \approx 2.2$ is not a spurious result caused by the slight rise in daytime median CTH observed at that point, which could affect the N_i retrieval via a decrease in temperature. The implications of the N_i evolution observed here are discussed in the following section.

4. Discussion

The findings presented in section 3 offer strong support for the selective cloud maintenance hypothesis proposed by Hartmann and Berry (2017). Anvil clouds with an optical depth between 1 and 2 ("modal anvils") are especially abundant in convective regions and are uniquely capable of persisting far from any convective core. This suggests that the mechanisms that maintain anvil clouds are most active within the modal τ range and that optically thicker clouds will continue to thin until the modal τ is reached. We find that most of this thinning occurs within ~60 km of the convective core, beyond which the cloud distribution becomes increasingly dominated by modal anvils. Past work suggests that the initial optical thinning is driven by dynamic outflow collapse (Lilly, 1988) and by the fallout of large ice crystals (e.g., Gallagher et al., 2012;

Jensen et al., 2018). We find evidence for both of these mechanisms and hypothesize that radiative heating can influence the thinning of freshly detrained anvils by hastening cloud-top subsidence at night and hindering it during the day.

Our findings also offer insight into the physical mechanisms responsible for the maintenance of modal anvils. Modal anvils undergo stronger radiative heating and have higher cloud tops than thicker anvils, which is consistent with the mesoscale lofting of the cloud with respect to its clear-sky surroundings. However, it is puzzling that modal anvil tops are found at lower altitudes during the day than at night despite the fact that there is stronger radiative heating during the day. It is possible that most of the modal anvils observed at 01:30 were detrained during the day, when solar heating would have hindered cloud-top subsidence and geometric thinning. As they age, they could retain the higher CTH and thicker geometry relative to anvils detrained at night (but observed at 13:30) that underwent faster geometric thinning due to cloud-top cooling. This explanation suggests that the life cycle of convective outflow is subject to hysteresis, in which the initial evolution of a freshly detrained cloud influences its properties later on. It could then be the case that the large increase in 01:30 median CTH as τ approaches the modal range represents a shift in the anvil cloud population from those that were detrained at night to those detrained during the previous day.

Additionally, we find that the modal anvils observed at 13:30 are subjected to strong radiative destabilization and have higher cloud-top N_i than optically thicker clouds. This is consistent with the microphysical cycling mechanism of anvil maintenance, in which radiatively driven turbulence maintains or increases N_i by driving new ice crystal nucleation, counteracting sedimentation, or some combination thereof (Hartmann et al., 2018). It is also possible that the enhanced N_i is another example of the timing effect described previously: Since anvils are detrained with higher N_i at night, the N_i resurgence at modal τ at 13:30 may simply reflect a transition from fresher, optically thick clouds detrained during the day to aged, thin clouds detrained during the previous night. Even if this were the case, the high N_i in modal anvils would still reflect an impressive preservation of ice crystal number against sedimentation over large distances and timescales. The maintenance of cloud ice is also supported by our finding that r_e and IWC are approximately constant at a fixed altitude for τ below $\sim$5–10, most notably during the day. This suggests that the loss of ice due to gravity is being slowed and offers further support for the importance of in-cloud turbulence.

If destabilization is critical to cloud maintenance, it is possible that the thinner geometry of modal anvils observed during the day results from natural selection. Thinner anvils would be better suited to withstand the stabilization imparted by solar heating, since LW destabilization is greater in thinner clouds than in thicker clouds of equal τ. At night, in the absence of solar heating, such a thin geometry would not be required to achieve the same net destabilization. It may be that the diurnal difference in anvil structure results partly from this selection and partly from the hysteresis described previously.

Past work provides a theoretical framework for understanding the relative importance of mesoscale lofting and in-cloud convective mixing in the cirrus response to radiative heating. Mixing is favored over lofting when the cloud is horizontally extensive, cloud-base Q_R is strong, and the static stability of the environment is low (Garrett et al., 2005; Schmidt & Garrett, 2013). Modal anvils are wider than freshly detrained anvils and undergo especially strong heating at cloud base during the day. Furthermore, their typical CBH of $\sim$12 km coincides with a relative minimum in static stability, as calculated from ERA-Interim reanalysis for the study region. For these reasons, modal anvils may be more susceptible to in-cloud convection than their fresh, optically thick precursors, which are narrower and are surrounded at their bases by a more stable environment. Following Garrett et al. (2005), the relative importance of the two mechanisms can be determined by the ratio $Q_R L/Nh^2(d\theta/dz)$, where L is the anvil half-width, N is the environmental buoyancy frequency, h is the depth of the heated layer at cloud base, and θ is potential temperature. Our results indicate that h is on the order of $\sim$1 km, and typical values of N (0.009 s^{-1}) and $d\theta/dz$ (3 K km^{-1}) are derived from ERA-Interim reanalysis. We test a range of values for Q_R between 10 and 20 K day^{-1} and for L between 20 and 100 km and find that the ratio falls between 0.1 and 0.9. This suggests that both mesoscale lofting and in-cloud convection play important roles in the anvil response to radiative heating.

While this study has focused on radiative heating as a driver of anvil cloud evolution, it is important to remember that other processes are at play. Numerical models indicate that latent heating is substantial, especially at the edges of freshly detrained anvils where ice crystals can readily sublimate (Gasparini et al., 2019). Additionally, anvil clouds may respond to radiative heating in ways not discussed here. For

example, Schmidt and Garrett (2013) found that tenuous cirrus clouds may evaporate in response to radiative heating, especially when there is high static stability.

5. Summary and Conclusions

We have provided a observational assessment of the macrophysical and microphysical evolution of tropical anvil clouds. Clouds associated with deep convection impart a distinct signature on the climatological distribution of cloud layer IWP that allows them to be distinguished from the thin cirrus clouds that blanket the tropical upper troposphere. Using a combined radar-lidar retrieval, we find that cirrus clouds layers with $1 < \tau < 2$ ("modal anvils") are especially prevalent across two maritime convective regions. Modal anvils have the following characteristics:

- They can persist several hundred kilometers away from a convective core and dominate the anvil cloud distribution at spreading distances greater than ∼60 km.
- They have higher cloud tops than optically thicker anvils. This lofting is especially pronounced at night.
- They are subjected to stronger net radiative heating than optically thick anvils. Modal anvils undergo LW heating throughout their entirety, whereas optically thicker clouds experience cloud-top cooling.
- They are geometrically thinner at 13:30 than at 01:30, with a 600-m difference in median thickness. The thinner geometry of modal anvils observed during the day renders them particularly prone to radiative destabilization.
- This daytime destabilization is associated with enhanced N_i at cloud top. At night, when modal anvils are geometrically thicker and less susceptible to radiative destabilization, the N_i resurgence is correspondingly weaker.

These findings are in agreement with the hypothesis that anvil clouds with a positive NCRE are selectively maintained by radiative heating. They are also consistent with two proposed mechanisms of anvil maintenance: microphysical cycling, in which radiatively driven turbulence prevents the depletion of cloud ice, and mesoscale lofting, in which the cloud as a whole rises with respect to its surroundings. We have further hypothesized that the properties of aged anvil clouds are determined in part by the time of day at which they were first detrained. The rapid geometric thinning of anvil clouds detrained at night may facilitate stronger radiative heating and destabilization later on. Meanwhile, the slower thinning of anvil clouds detrained during the day allows their tops to persist at higher altitudes but results in weaker heating. Hysteresis could have important implications for anvil cloud evolution in a changing climate and is worthy of further study using cloud-resolving models that include a realistic diurnal cycle of insolation.

The present study underscores the importance of radiative, dynamic, and microphysical processes in determining the NCRE in tropical convective regions. Future work should focus on how the cloud maintenance processes examined here interact with other changes that are expected to result from greenhouse gas warming. In a warmer world, tropical convection is expected to be more aggregated (Emanuel et al., 2014), and anvil clouds are expected to move upward in altitude (Hartmann & Larson, 2002), where they may encounter an increasingly stable environment (Zelinka & Hartmann, 2010). The impact of these changes on high cloud fraction remains uncertain, with some models predicting varying degrees of reduction (Bony et al., 2016; Li et al., 2019; Tompkins & Craig, 1999) and others predicting an increase (Ohno et al., 2019). Discussions of future anvil cloud amount have typically focused on changes in the amount of convective detrainment; our results show that postdetrainment maintenance processes must also be considered.

Data Availability Statement

DARDAR data were obtained from the ICARE Data and Services Center (http://www.icare.univ-lille1.fr/projects/dardar), and MODIS data were from the NASA Level-1 and Atmosphere Archive and Distribution System (https://ladsweb.modaps.eosdis.nasa.gov). The derived data and radiative heating model results needed to reproduce the figures in this paper are available online (at http://hdl.handle.net/1773/45556).

References

Ackerman, T. P., Liou, K. N., Valero, F. P. J., & Pfister, L. (1988). Heating rates in tropical anvils. *Journal of the Atmospheric Sciences*, *45*(10), 1606–1623. https://doi.org/10.1175/1520-0469(1988)045<1606:HRITA>2.0.CO;2
Berry, E., & Mace, G. G. (2014). Cloud properties and radiative effects of the Asian summer monsoon derived from A-Train data. *Journal of Geophysical Research*, *119*, 9492–9508. https://doi.org/10.1002/2014JD021458

Bony, S., Stevens, B., Coppin, D., Becker, T., Reed, K. A., Voigt, A., & Medeiros, B. (2016). Thermodynamic control of anvil cloud amount. *Proceedings of the National Academy of Sciences of the United States of America*, *113*, 8927–8932. https://doi.org/10.1073/pnas.1601472113

Bretherton, C. S., Blossey, P. N., & Khairoutdinov, M. (2005). An energy-balance analysis of deep convective self-aggregation above uniform SST. *Journal of the Atmospheric Sciences*, *62*, 4273–4292. https://doi.org/10.1175/JAS3614.1

Cazenave, Q., Ceccaldi, M., Delanoë, J., Pelon, J., Groß, S., & Heymsfield, A. (2019). Evolution of DARDAR-CLOUD ice cloud retrievals: New parameters and impacts on the retrieved microphysical properties. *Atmospheric Measurement Techniques*, *12*(5), 2819–2835. https://doi.org/10.5194/amt-12-2819-2019

Delanoë, J., & Hogan, R. J. (2008). A variational scheme for retrieving ice cloud properties from combined radar, lidar, and infrared radiometer. *Journal of Geophysical Research*, *113*, D07204. https://doi.org/10.1029/2007JD009000

Delanoë, J., & Hogan, R. J. (2010). Combined CloudSat-CALIPSO-MODIS retrievals of the properties of ice clouds. *Journal of Geophysical Research*, *115*, D00H29. https://doi.org/10.1029/2009JD012346

Delanoë, J., Protat, A., Jourdan, O., Pelon, J., Papazzoni, M., Dupuy, R. A., et al. (2013). Comparison of airborne in situ, airborne radar lidar, and spaceborne radar lidar retrievals of polar ice cloud properties sampled during the POLARCAT campaign. *Journal of Atmospheric and Oceanic Technology*, *30*(1), 57–73. https://doi.org/10.1175/JTECH-D-11-00200.1

Deng, M., Mace, G. G., Wang, Z., & Paul Lawson, R. (2013). Evaluation of several A-Train ice cloud retrieval products with in situ measurements collected during the SPARTICUS campaign. *Journal of Applied Meteorology and Climatology*, *52*, 1014–1030. https://doi.org/10.1175/JAMC-D-12-054.1

Dinh, T. P., Durran, D. R., & Ackerman, T. P. (2010). Maintenance of tropical tropopause layer cirrus. *Journal of Geophysical Research*, *115*, D02104. https://doi.org/10.1029/2009JD012735

Dobbie, S., & Jonas, P. (2001). Radiative influences on the structure and lifetime of cirrus clouds. *Quarterly Journal of the Royal Meteorological Society*, *127*(578), 2663–2682. https://doi.org/10.1002/qj.49712757808

Durran, D. R., Dinh, T., Ammerman, M., & Ackerman, T. (2009). The mesoscale dynamics of thin tropical tropopause cirrus. *Journal of the Atmospheric Sciences*, *66*(9), 2859–2873. https://doi.org/10.1175/2009JAS3046.1

Emanuel, K., Wing, A. A., & Vincent, E. M. (2014). Radiative-convective instability. *Journal of Advances in Modeling Earth Systems*, *6*, 75–90. https://doi.org/10.1002/2013MS000270

Fu, Q. (1996). An accurate parameterization of the solar radiative properties of cirrus clouds for climate models. *Journal of Climate*, *9*(9), 2058–2082. https://doi.org/10.1175/1520-0442(1996)009<2058:AAPOTS>2.0.CO;2

Fu, Q., Yang, P., & Sun, W. B. (1998). An accurate parameterization of the infrared radiative properties of cirrus clouds for climate models. *Journal of Climate*, *11*(9), 2223–2237. https://doi.org/10.1175/1520-0442(1998)011<2223:AAPOTI>2.0.CO;2

Gallagher, M. W., Connolly, P. J., Crawford, I., Heymsfield, A., Bower, K. N., Choularton, T. W., et al. (2012). Observations and modelling of microphysical variability, aggregation and sedimentation in tropical anvil cirrus outflow regions. *Atmospheric Chemistry and Physics*, *12*(14), 6609–6628. https://doi.org/10.5194/acp-12-6609-2012

Garrett, T. J., Navarro, B. C., Twohy, C. H., Jensen, E. J., Baumgardner, D. G., Bui, P. T., et al. (2005). Evolution of a Florida cirrus anvil. *Journal of the Atmospheric Sciences*, *62*(7 II), 2352–2372. https://doi.org/10.1175/JAS3495.1

Gasparini, B., Blossey, P. N., Hartmann, D. L., Lin, G., & Fan, J. (2019). What drives the lifecycle of tropical anvil clouds? *Journal of Advances in Modeling Earth Systems*, *11*, 2019MS001736. https://doi.org/10.1029/2019MS001736

Gettelman, A., Salby, M. L., & Sassi, F. (2002). Distribution and influence of convection in the tropical tropopause region. *Journal of Geophysical Research*, *107*(D10). https://doi.org/10.1029/2001JD001048

Harrison, E. F., Minnis, P., Barkstrom, B. R., Ramanathan, V., Cess, R. D., & Gibson, G. G. (1990). Seasonal variation of cloud radiative forcing derived from the Earth Radiation Budget Experiment. *Journal of Geophysical Research*, *95*(D11), 18,687–18,703. https://doi.org/10.1029/JD095id11p18687

Hartmann, D. L. (2016). Tropical anvil clouds and climate sensitivity. https://doi.org/10.1073/pnas.1610455113

Hartmann, D. L., & Berry, S. E. (2017). The balanced radiative effect of tropical anvil clouds. *Journal of Geophysical Research: Atmospheres*, *122*, 5003–5020. https://doi.org/10.1002/2017JD026460

Hartmann, D. L., Gasparini, B., Berry, S. E., & Blossey, P. N. (2018). The life cycle and net radiative effect of tropical anvil clouds. *Journal of Advances in Modeling Earth Systems*, *10*, 3012–3029. https://doi.org/10.1029/2018MS001484

Hartmann, D. L., & Larson, K. (2002). An important constraint on tropical cloud-climate feedback. *Geophysical Research Letters*, *29*, 1951. https://doi.org/10.1029/2002GL015835

Hartmann, D. L., Moy, L. A., & Fu, Q. (2001). Tropical convection and the energy balance at the top of the atmosphere. *Journal of Climate*, *14*, 4495–4511. https://doi.org/10.1175/1520-0442(2001)014<4495:TCATEB>2.0.CO;2

Heymsfield, A. J., Bansemer, A., Field, P. R., Durden, S. L., Stith, J. L., Dye, J. E., et al. (2002). Observations and parameterizations of particle size distributions in deep tropical cirrus and stratiform precipitating clouds: Results from in situ observations in TRMM field campaigns. *Journal of the Atmospheric Sciences*, *59*(24), 3457–3491. https://doi.org/10.1175/1520-0469(2002)059<3457:OAPOPS>2.0.CO;2

Iacono, M. J., Mlawer, E. J., Clough, S. A., & Morcrette, J.-J. (2000). Impact of an improved longwave radiation model, RRTM, on the energy budget and thermodynamic properties of the NCAR community climate model, CCM3. *Journal of Geophysical Research*, *105*(D11), 14,873–14,890. https://doi.org/10.1029/2000JD900091

Igel, M. R., Drager, A. J., & van den Heever, S. C. (2014). A CloudSat cloud object partitioning technique and assessment and integration of deep convective anvil sensitivities to sea surface temperature. *Journal of Geophysical Research: Atmospheres*, *119*, 10,515–10,535. https://doi.org/10.1002/2014JD021717

Järvinen, E., Jourdan, O., Neubauer, D., Yao, B., Liu, C., Andreae, M. O., et al. (2018). Additional global climate cooling by clouds due to ice crystal complexity. *Atmospheric Chemistry and Physics*, *18*(21), 15,767–15,781. https://doi.org/10.5194/acp-18-15767-2018

Jensen, E. J., Lawson, P., Baker, B., Pilson, B., Mo, Q., Heymsfield, A. J., et al. (2009). On the importance of small ice crystals in tropical anvil cirrus. *Atmospheric Chemistry and Physics*, *9*, 5519–5537. https://doi.org/10.5194/acp-9-5519-2009

Jensen, E. J., van den Heever, S. C., & Grant, L. D. (2018). The life cycles of ice crystals detrained from the tops of deep convection. *Journal of Geophysical Research: Atmospheres*, *123*, 9624–9634. https://doi.org/10.1029/2018JD028832

Krämer, M., Rolf, C., Spelten, N., Afchine, A., Fahey, D., Jensen, E., et al. (2020). A microphysics guide to cirrus—Part II: Climatologies of clouds and humidity from observations. *Atmospheric Chemistry and Physics*. https://doi.org/10.5194/acp-2020-40

Lawson, R. P., Jensen, E., Mitchell, D. L., Baker, B., Mo, Q., & Pilson, B. (2010). Microphysical and radiative properties of tropical clouds investigated in TC4 and NAMMA. *Journal of Geophysical Research*, *115*, D00J08. https://doi.org/10.1029/2009JD013017

Li, R. L., Storelvmo, T., Fedorov, A. V., & Choi, Y.-S. (2019). A positive Iris feedback: Insights from climate simulations with temperature-sensitive cloud rain conversion. *Journal of Climate*, *32*(16), 5305–5324. https://doi.org/10.1175/JCLI-D-18-0845.1

Lilly, D. K. (1988). Cirrus outflow dynamics. *Journal of the Atmospheric Sciences*, *45*(10), 1594–1605. https://doi.org/10.1175/1520-0469(1988)045<1594:COD>2.0.CO;2

Luo, Z., & Rossow, W. B. (2004). Characterizing tropical cirrus life cycle, evolution, and interaction with upper-tropospheric water vapor using Lagrangian trajectory analysis of satellite observations. *Journal of Climate*, *17*(23), 4541–4563. https://doi.org/10.1175/3222.1

Mace, G. G., Deng, M., Soden, B., & Zipser, E. (2006). Association of tropical cirrus in the 10–15-km layer with deep convective sources: An Observational study combining millimeter radar data and satellite-derived trajectories. *Journal of the Atmospheric Sciences*, *63*(2), 480–503. https://doi.org/10.1175/JAS3627.1

Massie, S., Gettelman, A., Randel, W., & Baumgardner, D. (2002). Distribution of tropical cirrus in relation to convection. *Journal of Geophysical Research*, *107*(D21), 4591. https://doi.org/10.1029/2001JD001293

McFarquhar, G. M., & Heymsfield, A. J. (1996). Microphysical characteristics of three anvils sampled during the central equatorial Pacific experiment. *Journal of the Atmospheric Sciences*, *53*(17), 2401–2423. https://doi.org/10.1175/1520-0469(1996)053<2401:MCOTAS>2.0.CO;2

McFarquhar, G. M., Heymsfield, A. J., Spinhirne, J., & Hart, B. (1999). Thin and subvisual tropopause tropical cirrus: Observations and radiative impacts. *Journal of the Atmospheric Sciences*, *57*(12), 1841–1853. https://doi.org/10.1175/1520-0469(2000)057<1841:TASTTC>2.0.CO;2

McGill, M. J., Vaughan, M. A., Trepte, C. R., Hart, W. D., Hlavka, D. L., Winker, D. M., & Kuehn, R. (2007). Airborne validation of spatial properties measured by the CALIPSO lidar. *Journal of Geophysical Research*, *112*, D20201. https://doi.org/10.1029/2007JD008768

Mlawer, E. J., Taubman, S. J., Brown, P. D., Iacono, M. J., & Clough, S. A. (1997). Radiative transfer for inhomogeneous atmospheres: RRTM, a validated correlated-k model for the longwave. *Journal of Geophysical Research*, *102*(D14), 16,663–16,682. https://doi.org/10.1029/97JD00237

Nesbitt, S. W., & Zipser, E. J. (2003). The diurnal cycle of rainfall and convective intensity according to three years of TRMM measurements. *Journal of Climate*, *16*(10), 1456–1475. https://doi.org/10.1175/1520-0442-16.10.1456

Ohno, T., Satoh, M., & Noda, A. (2019). Fine vertical resolution radiative convective equilibrium experiments: Roles of turbulent mixing on the high cloud response to sea surface temperatures. *Journal of Advances in Modeling Earth Systems*, *11*, 1637–1654. https://doi.org/10.1029/2019MS001704

Platnick, S., Meyer, K. G., King, M. D., Wind, G., Amarasinghe, N., Marchant, B., et al. (2017). The MODIS cloud optical and microphysical products: Collection 6 updates and examples from Terra and Aqua. *IEEE Transactions on Geoscience and Remote Sensing*, *55*(1), 502–525. https://doi.org/10.1109/TGRS.2016.2610522

Ramanathan, V., Cess, R. D., Harrison, E. F., Minnis, P., Barkstrom, B. R., Ahmad, E., & Hartmann, D. (1989). Cloud-radiative forcing and climate: Results from the earth radiation budget experiment. *Science*, *243*(4887), 57–63. https://doi.org/10.1126/science.243.4887.57

Randall, D. A., Harshvardhan, Dazlich, D. A., & Corsetti, T. G. (1989). Interactions among radiation, convection, and large-scale dynamics in a general circulation model. *Journal of the Atmospheric Sciences*, *46*, 1943–1970. https://doi.org/10.1175/1520-0469(1989)046<1943:IARCAL>2.0.CO;2

Schmidt, C. T., & Garrett, T. J. (2013). A simple framework for the dynamic response of cirrus clouds to local diabatic radiative heating. *Journal of the Atmospheric Sciences*, *70*(5), 1409–1422. https://doi.org/10.1175/JAS-D-12-056.1

Setvák, M., Rabin, R. M., & Wang, P. K. (2006). Contribution of the MODIS instrument to observations of deep convective storms and stratospheric moisture detection in GOES and MSG imagery. *Atmospheric Research*, *83*, 505–518. https://doi.org/10.1016/j.atmosres.2005.09.015

Sourdeval, O., Gryspeerdt, E., Krämer, M., Goren, T., Delanoë, J., Afchine, A., et al. (2018). Ice crystal number concentration estimates from lidar-radar satellite remote sensing—Part 1: Method and evaluation. *Atmospheric Chemistry and Physics*, *18*, 14,327–14,350. https://doi.org/10.5194/acp-18-14327-2018

Stein, T. H. M., Delanoë, J., & Hogan, R. J. (2011). A comparison among four different retrieval methods for ice-cloud properties using data from CloudSat, CALIPSO, and MODIS. *Journal of Applied Meteorology and Climatology*, *50*(9), 1952–1969. https://doi.org/10.1175/2011JAMC2646.1

Stephens, G. L., Vane, D. G., Boain, R. J., Mace, G. G., Sassen, K., Wang, Z., et al. (2002). The CloudSat mission and the A-Train: A new dimension of space-based observations of clouds and precipitation. *Bulletin of the American Meteorological Society*, *83*(12), 1771–1790. https://doi.org/10.1175/BAMS-83-12-1771

Tompkins, A. M., & Craig, G. C. (1999). Sensitivity of tropical convection to sea surface temperature in the absence of large-scale flow. *Journal of Climate*, *12*, 462–476. https://doi.org/10.1175/1520-0442(1999)012<0462:SOTCTS>2.0.CO;2

Voigt, A., & Shaw, T. A. (2015). Circulation response to warming shaped by radiative changes of clouds and water vapour. *Nature Geoscience*, *8*, 102–106. https://doi.org/10.1038/ngeo2345

Wall, C. J., Hartmann, D. L., & Norris, J. R. (2019). Is the net cloud radiative effect constrained to be uniform over the tropical warm pools? *Geophysical Research Letters*, *46*, 12,495–12,503. https://doi.org/10.1029/2019GL083642

Wall, C. J., Hartmann, D. L., Thieman, M. M., Smith, W. L., & Minnis, P. (2018). The life cycle of anvil clouds and the top-of-atmosphere radiation balance over the tropical West Pacific. *Journal of Climate*, *31*(24), 10,059–10,080. https://doi.org/10.1175/JCLI-D-18-0154.1

Wendisch, M., Yang, P., & Pilewskie, P. (2007). Effects of ice crystal habit on thermal infrared radiative properties and forcing of cirrus. *Journal of Geophysical Research*, *112*, D08201. https://doi.org/10.1029/2006JD007899

Wing, A. A., & Emanuel, K. A. (2014). Physical mechanisms controlling self-aggregation of convection in idealized numerical modeling simulations. *Journal of Advances in Modeling Earth Systems*, *6*, 59–74. https://doi.org/10.1002/2013MS000269

Winker, D. M., Pelon, J., Coakley, J. A., Ackerman, S. A., Charlson, R. J., Colarco, P. R., et al. (2010). The CALIPSO mission. *Bulletin of the American Meteorological Society*, *91*(9), 1211–1230. https://doi.org/10.1175/2010BAMS3009.1

Winker, D. M., & Trepte, C. R. (1998). Laminar cirrus observed near the tropical tropopause by LITE. *Geophysical Research Letters*, *25*(17), 3351–3354. https://doi.org/10.1029/98GL01292

Young, A. H., Bates, J. J., & Curry, J. A. (2012). Complementary use of passive and active remote sensing for detection of penetrating convection from CloudSat, CALIPSO, and Aqua MODIS. *Journal of Geophysical Research*, *117*, D13205. https://doi.org/10.1029/2011JD016749

Yuan, J., & Houze, R. A. (2010). Global variability of mesoscale convective system anvil structure from A-train satellite data. *Journal of Climate*, *23*(21), 5864–5888. https://doi.org/10.1175/2010JCLI3671.1

Yuan, J., Houze, R. A., & Heymsfield, A. J. (2011). Vertical structures of anvil clouds of tropical mesoscale convective systems observed by CloudSat. *Journal of the Atmospheric Sciences*, *68*(8), 1653–1674. https://doi.org/10.1175/2011JAS3687.1

Zelinka, M. D., & Hartmann, D. L. (2010). Why is longwave cloud feedback positive? *Journal of Geophysical Research*, *115*, D16117. https://doi.org/10.1029/2010JD013817